

# INITIAL CONDITION EFFECTS ON KELVIN-HELMHOLTZ INSTABILITIES AND DEVELOPMENT OF A ROUND JET

**Amy B. McCleney and Philippe M. Bardet**

The George Washington University  
800 22<sup>nd</sup> St NW, Washington, D.C. 20037  
mccleney@gwu.edu; bardet@gwu.edu

## ABSTRACT

The effect of initial velocity profile of a round, axisymmetric, incompressible jet in the self-preserving regime is studied with optical diagnostics. The jet discharges freely into a large tank and two Reynolds numbers of 10,000 and 20,000 are analyzed. Jet near- and far-field behaviors are instrumented with a combination of planar laser induced fluorescence and time-resolved particle image velocimetry. In the near field, shear layer roll-up is analyzed and characterized as a function of initial velocity profile. Turbulent statistics in the self-similar regime are reported for a neutrally buoyant jet at near Taylor microscale resolution. It is found that independent of initial conditions, the jet tends to follow a self-similar behavior in the far field; however, the spreading rate is strongly dependent on initial velocity profile. The facility enables the establishment of a stratification in the tank. In this case, to prevent optical aberration and provide high spatial resolution data, index matched fluids are employed.

## KEYWORDS

Turbulence, Round Jet, Kelvin Helmholtz instabilities, Initial Conditions Effects, Validation

## 1. INTRODUCTION

Jets have been extensively studied due to their presence in environmental and industrial applications. In environmental flows, hydrothermal plumes and wastewater discharging from pipes are examples of one fluid being introduced into another. Round jets are also used for fuel injection in internal combustion engine cylinders [1] and in liquid rocket engines [2]. Jets that interact with a stratified layer are also important in accident conditions in containment buildings of nuclear reactors. There, jets and plumes mix and transfer gases, which strongly influence the development of accidents and is thus important for the safety of nuclear reactors [3].

When a moving fluid, or jet, is injected into a quiescent fluid, velocity gradients develop. Initially, this shear can cause a roll-up of the jet boundary layer creating vortex rings in the case of cylindrical jets [4]. This phenomenon is known as Kelvin-Helmholtz (KH) instabilities [5]. These vortex rings entrain the surrounding fluid, and tend to interact with each other, which causes mixing and turbulence [6]. Their evolution and interaction creates a complex three-dimensional turbulent flow field that eventually reaches self-similarity in the far-field.

KH instabilities are modeled assuming a perturbation is developed at the flow interface, which results in a complex dispersion relationship describing an exponentially decaying or growing solution [7]. This growth is based on the instability frequency and is directly proportional to the velocity difference between the jet and surrounding fluid. Therefore, the frequency increases with the jet velocity, causing the roll-up

of the boundary layer into vortex rings to occur in shorter time intervals. The development of the boundary layer is also dependent on both viscous and inertial forces [8]. With an increase in velocity, inertial forces become dominant, causing the boundary layer thickness to be thinner or smaller. This results in KH instabilities which yield smaller vortex rings which shed or form at a higher frequencies.

Incompressible jets are extremely sensitive to their initial conditions, which latter alters the flow formation and evolution. They are influenced by effects such as Reynolds number and nozzle geometric profiles. In a theoretical analysis focused on jet evolution into a self-preserving state, George [9] noted that turbulent flows can asymptotically reach self-similar behavior, but that this state strongly depends on initial conditions. Quinn [10] examined the effects of nozzle shape on jet evolution using the same exit Reynolds number. He showed that the centerline velocity decay rate is much higher in a jet that is initiated from a sharp-edged orifice compared to one initiated from a contoured nozzle. Ferman et al. [11] experimentally investigated the effects of non-uniform initial velocity profiles on turbulent jet evolution. This was accomplished for both an axisymmetric fully-developed velocity profile and an axisymmetric initial velocity profile. They noted that the slope of the centerline velocity decay is much higher for the fully-developed case, but both jets appeared to have identical behavior in the far-field, with the same self-similar mean-velocity profiles.

Mi et al. [12] examined the flow field of two different profiled jets, one with a top-hat, and one which is fully-developed from pipe flow. They concluded that in both the near- and far-field, the turbulent scalar properties are dependent on the initial conditions, where vortical structures that enhance both the entrainment and mixing processes are almost absent in the fully-developed flow case. Xu and Antonia [13] also compared jet characteristics with similar velocity profiles at the nozzle exit. In contrast to the study conducted by Mi et al., they noted that the jet with the top-hat profile reached a self-similar state more rapidly than the pipe flow profile.

To study the effect of initial conditions on both the near- and far-field, an experimental vertical round jet is employed, where flow conditioning prior to jet initiation is altered for fixed Reynolds numbers,  $Re$ . The flow is investigated with a combination of planar laser induced fluorescence (PLIF) and time-resolved particle image velocimetry (PIV). Near-field evaluation of the shedding frequencies of vortex rings from jet instabilities and mean axial velocity profiles are examined and compared for each flow rate. Velocity profiles are analyzed in the far-field, 30 to 50 nozzle diameters downstream of the exit, where the jet is considered self-similar for the high  $Re$  case.

## 2. EXPERIMENTAL FACILITY AND APPARATUS

The vertically oriented test facility produces a round, axisymmetric, incompressible jet with controllable velocity, with low-level of initial disturbances, Fig. 1 (a). The displacement of a piston through a cylinder generates the axial flow. A linear motor provides motion and control of the piston. Since the fluid in the cylinder is initially at rest, the issuing flow has little to no initial disturbances and flow conditioning is not necessary; hence, the initial conditions are precisely known and controlled. After the cylindrical chamber, diameter of 203 mm, the fluid goes through a first contraction followed by a second contoured nozzle, with exit diameter,  $D$ , of 12.7 mm, into a large square tank. The aspect ratio of each contraction section is identical and is 16 to 1. The tank has a width to nozzle diameter ratio of 72. This large ratio guarantees no interaction between the jet and the side walls. The tank is made of clear acrylic and allows for visual access to the flow. The piston and contraction sections are encased in a cylindrical chamber which is connected to the bottom of the tank. Full details of the experiment facility design can be found in McCleney [14].

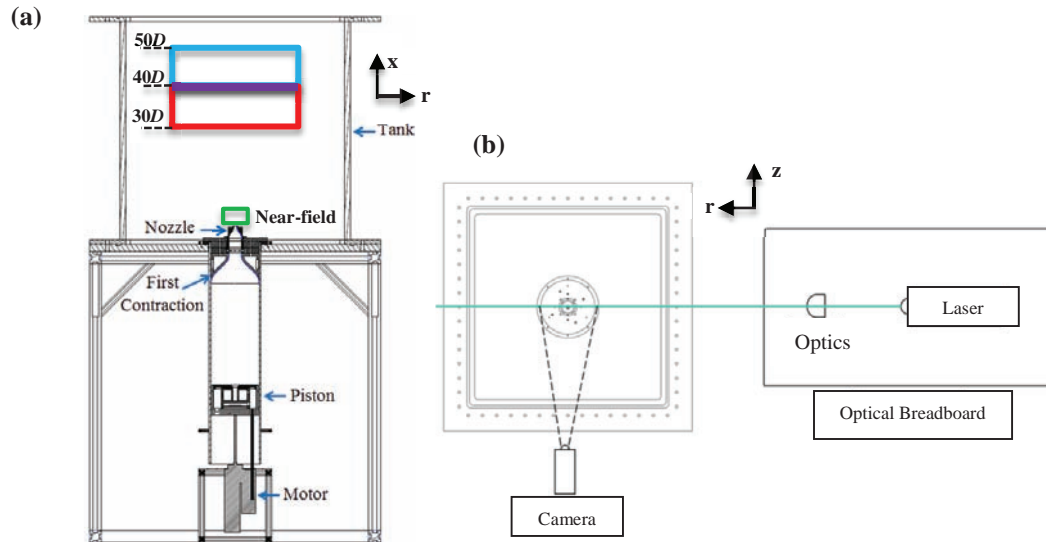


**Figure 1. (a) Side view of the highly repeatable experimental vertical water tunnel facility. Flow measurements are taken in the near-field right outside the nozzle exit, indicated by green area. Flow measurements in the far-field are obtained using two PIV frames, blue and red area, with overlapped measurements at  $40D$  (b) Top view of optical configuration.**

Since the facility utilizes a free surface, the jet can be subjected to recirculation in the confined facility, which can alter the entrainment or jet growth. Analysis on the effect of confinement on momentum conservation due to the tank walls and height of the free surface [15] shows that this recirculation effect has little impact on the jet, at measurement locations up to  $50D$ , where the experimental jet closely resembles a jet in an infinite environment. The experimental facility has been extensively characterized and produces a jet with little to no initial disturbances. Introduction of low level disturbances introduced by the piston and cylinder were shown to be minimal above a  $Re$  of 2,000 and does not affect the jet structures for the high Reynolds number data presented here. The motor is controlled with a position accuracy of  $2\ \mu\text{m}$ , which allows for precise control of the piston mean flow through the cylindrical chamber within  $7 \times 10^{-2}\ \mu\text{m/s}$ . Above  $Re$  of 2,000, the jet formation and velocity profiles are consistently reproduced as indicated by multiple test samples and analysis at various flow rates.

To alter the jet initial velocity profile, two screens can be inserted between the first and second contoured nozzle. Screens reduce the velocity defect in boundary layers that pass through it, and improves the mean flow uniformity [16]. With no screens, a thick boundary layer develops along the wall of the cylinder and the contraction sections and leads to a jet with a profile that is close to being parabolic. The two screens minimize the boundary layer thickness of the jet to generate a top-hat profile at the second nozzle exit. The boundary layer thickness,  $\delta$ , at the nozzle exit is estimated through the experimental facility with an iterative process. An axisymmetric Thwaites approximation is employed to estimate the boundary layer thickness at any location in the chamber. The initial boundary layer is assumed to have zero thickness at the top of the piston. The flow away from the wall is assumed to have a plug profile and its velocity is corrected for to conserve mass by taking into account contractions in the chamber and the estimated boundary layer displacement thickness. The process is repeated till boundary layer momentum thickness converges. The two screens are located in series from a coarse mesh,  $32 \times 32$  with an open area ratio of 63%, to a fine mesh,  $42 \times 42$  with a 59% open area ratio, and are spaced by 25.4 mm. The flow redistribution can be estimated and related to pressure drop through the mesh [17], which leads to new estimates for the boundary layers at the exit of the nozzle.

Turbulent round jets are observed for two different Re values for the top-hat and parabolic jet. Re is a dimensionless parameter, Eq.1, and is characterized by the mean velocity at the nozzle exit,  $U_0$ , and  $D$ . The velocity initiated by the piston is chosen so conservation of mass through the experiment yields an exit velocity that is approximately  $U_0$ .  $U_0$  used in this study is 0.787 m/s and 1.57 m/s, and results in a Re of 10,000 and 20,000. At these flow rates the jet run time is around 60 s for Re of 10,000 and 30 s for the higher Re case for one full stroke of the piston.

$$\text{Re} = \frac{U_0 D}{\nu} \quad (1)$$

To obtain velocity fields and visualize the mechanics of the flow-field, water is used as the working fluid for both qualitative and quantitative measurements. Fluorescein dye, used for flow visualization with PLIF, is introduced either azimuthally into the jet boundary layer at the entrance of the second nozzle or by dissolving it homogeneously in the chamber to mark the jet. For PIV, both the surrounding fluid and the jet are seeded with 30  $\mu\text{m}$  diameter particles. The same laser and camera are used either for PLIF or PIV. They are positioned perpendicular to each other, Fig. 1 (b), with the laser illuminating a plane in the center of the jet. The laser is an Argon-Ion CW laser operated at 1W. A sheet is formed using a cylindrical and spherical lens and has a beam waist,  $\omega_0$ , estimated at 0.65 mm and a Rayleigh range, half the length over which the laser sheet cross section area increases by  $\sqrt{2}$ , of 77 mm estimated by taking into account the effect of water on light convergence and the laser beam quality or  $M^2$ . The flow structures are captured and recorded with an IDT NX3-S3 CMOS camera, which has a dynamic range of 10 bits at 1280 by 1024 pixels, with a maximum frame rate of 2,500 frames per second at full resolution.

Characteristics for imaging diagnostics for PLIF and PIV are noted in Table I and Table II. PLIF is conducted in the jet near-field, Fig. 1 (a), to observe and analyze vortex behavior evolving from the nozzle exit with change in velocity profile. This is accomplished for both Re = 10,000 and 20,000 at a magnification,  $M$ , of 0.5 using a Nikon micro 200 mm  $f/4$  lens, at various frame rates and exposures. This enables the capturing of a number of vortex formation cycles that is case dependent and varies from 140 to 430.

**Table I. PLIF imaging characteristics for near-field for Re = 10,000 and 20,000 analysis**

	Re = 10,000		Re = 20,000	
	Top hat	Parabolic	Top hat	Parabolic
<b>Frame rate</b>	500 Hz	1,500 Hz	2,000 Hz	1,500 Hz
<b>Exposure</b>	1,000 $\mu\text{s}$	350 $\mu\text{s}$	140 $\mu\text{s}$	350 $\mu\text{s}$
<b>Frames</b>	1,500	3,000	3,000	3,000
<b>Formation Cycles</b>	375	140	430	416

PIV is accomplished in the near-field for Re = 10,000 for both the top hat and parabolic velocity profiles. PIV images are analyzed in a time-series manner. 3,000 images are used to obtain an overall averaged representation of the velocity at the nozzle exit, where approximately 150 cycles of shedding vortices are captured for each profile. Image calibration is accomplished using the nozzle geometry as a scaling parameter. Axial and fluctuating velocity profiles are generated at various fields of views and cross correlation window sizes. PIV diagnostics at Re = 20,000 is not accomplished in the near-field due to camera acquisition and light illumination limitations.

Two separate PIV frames are used to capture the jet in the far-field for Re = 20,000, one ranging from 30 to 40 nozzle diameters, and the second ranging from 40 to 50. The overlapped data, purple line in Fig.1(a), is analyzed separately for each PIV frame. 6,000 images are averaged to obtain an appropriate statistical representation of the jet, data are also analyzed in a time-series manner and hence are

correlated. Before jet initiation, a calibration target is positioned in the PIV imaging plane to correct image distortions, and then removed for testing. Far-field  $Re = 10,000$  PIV data are not reported here for conciseness.  $Re = 20,000$  is presented because analysis in the far-field is used for validation and comparison to a buoyant jet injected into a stratified environment at the same  $Re$  from the facility, Section 6. The uncertainty in the correlation method used in PIV is estimated to be around 1.6% for the bulk velocity of the jet. Errors due to calibration are negligible.

**Table II. PIV characteristics for near-field  $Re = 10,000$  analysis and far-field  $Re = 20,000$  analysis**

	<b>Re = 10,000</b>		<b>Re = 20,000</b>	
	<b>Top hat</b>	<b>Parabolic</b>	<b>Top hat</b>	<b>Parabolic</b>
<b>M</b>	0.31	0.27	0.1	0.12
<b>Camera lens</b>	105 mm $f/2.8$		50 mm $f/1.2$	
$\omega_0$	0.65 mm			
<b>Field of View</b>	44 × 35 mm	51 × 41 mm	140 × 111 mm	116 × 92 mm
<b>Frame rate</b>	2,500 Hz	1,500 Hz	250 & 200 Hz	150 & 125 Hz
<b>Exposure</b>	98 $\mu$ s	350 $\mu$ s	2,825 & 3,500 $\mu$ s	2,825 & 3,000 $\mu$ s
<b>Cross Correlation Widow size (multipass)</b>	64 × 64 24 × 24			
<b>Cross Correlation Widow size</b>	0.8 × 0.8 mm 0.18 $\lambda$ × 0.18 $\lambda$	1.0 × 1.0 mm 0.22 $\lambda$ × 0.22 $\lambda$	2.6 × 2.6 mm 0.59 $\lambda$ × 0.59 $\lambda$	2.2 × 2.2 mm 0.50 $\lambda$ × 0.50 $\lambda$
<b>Images</b>	3,000		6,000	

In the far-field, the centerline velocity, axial velocity, and Reynolds stress profiles are used to describe jet characteristics. For a self-preserving jet in the far-field, the centerline velocity is written with respect to the virtual origin,  $X_0$ , and the initial momentum flux,  $M_0$ , at the nozzle exit, Eq.2 [15].

$$U_c = BM_0^{1/2}/(X - X_0) \quad (2)$$

$B$  in Eq.2 is proportionality constant, while  $M_0$  is calculated from the nozzle exit diameter, and  $U_0$ , Eq.3.

$$\rho M_0 = \frac{1}{4} \pi U_0^2 D^2 \quad (3)$$

For a jet with an initial top-hat profile, the centerline velocity from Eq.2 and Eq.3, can be written, Eq.4.

$$\frac{U_0}{U_c} = \frac{1}{B_u} \left( \frac{X}{D} - \frac{X_0}{D} \right) \quad (4)$$

For top hat jet, the slope value,  $B_u$ , is dependent on the initial conditions and can be written in relation to  $B$ , Eq.5.

$$B_u = \frac{1}{2} \pi^{1/2} B \quad (5)$$

$B_u$ , in Eq.4 and Eq.5, is approximately 5.8 [18]. Although the velocity decay rate is consistent around this value for a jet initiated with a top hat profile, the virtual origin of the jet is dependent on the ratio between  $U_0$ , and the centerline velocity,  $U_c$ , and can slightly vary between facilities, such as with the facility of

Ferdman et al. [11], where  $X_0$  is around  $2.5D$ , which is closer to the nozzle exit compared to Xu and Antonia [13], where  $X_0$  is  $3.7D$ .

Turbulent flows are made up of a broad range of length scales. At the smallest length scale, the Kolmogorov scale,  $\eta$ , viscosity is dominant and turbulent kinetic energy is dissipated into heat, Eq.6 [18].

$$\eta = \left(\frac{\nu^3}{\varepsilon}\right)^{1/4} \quad (6)$$

The scale in Eq.6 is based on the kinematic viscosity and the turbulent kinetic energy dissipation rate,  $\varepsilon$ , which for round self-similar jets is, Eq.7 [18].

$$\varepsilon = 0.015 \frac{(U_c)^3}{r^{1/2}} \quad (7)$$

$\varepsilon$  in Eq.6 is based on the centerline velocity and the jets half-width,  $r^{1/2}$ . The energy dissipation rate is also used to describe the Taylor micro length scale,  $\lambda$ , Eq.8 [18].

$$\lambda = u' \sqrt{15 \frac{\nu}{\varepsilon}} \quad (8)$$

The Taylor microscale depends on the rms of axial velocity fluctuations,  $u'$ , and the ratio of the fluid kinematic viscosity and turbulent kinetic energy dissipation rate, where a commonly used quantity to characterize the level of turbulence is the Taylor-scale Reynolds number,  $Re_\lambda$ , Eq.9 [18].

$$Re_\lambda = \frac{u'\lambda}{\nu} \quad (9)$$

For self-similar jets, the turbulence statistics can be determined from large scale velocity field measurements. Using these length scales and velocity and Reynolds stress profiles, a turbulent round jet is characterized and compared for an initial top hat and parabolic profile to study initial condition effects of a jet in the self-similar regime and provide baseline for future tests with buoyant jet studies.

### 3. INITIAL VELOCITY PROFILES

Axial and fluctuating velocity profiles at various downstream positions for  $Re = 10,000$  is captured with PIV in the near-field. The boundary layer thickness right outside the nozzle exit,  $0.09 D$ , is measured starting at the radial position where the axial velocity begins to decrease in value from the centerline velocity, and ending at the location where the axial velocity reaches zero. For the top hat profile, initial axial and fluctuating velocity profiles are normalized by  $U_0$ , while the horizontal scale is normalized by the nozzle radius,  $R$ , Fig.2 (a) and (b). Axial profiles show a symmetric profile for all measurement locations, and the fluctuating velocities have higher values closer to the edge of the jet with a decrease in the centerline. As the distance from the nozzle exit increases, the overall fluctuating velocities grow slightly larger. The boundary layer thickness,  $\delta_{PIV}$ , obtained at  $X/D$  of 0.09, is 1.2 mm. This favorably agrees with the theoretically obtained  $\delta$  using screens at 1.4 mm.

For the same flow rate, but without screens, the round jet is initially still axisymmetric; however its boundary layer at the nozzle exit is very thick and the mean axial flow profile is almost parabolic, seen at  $X/D$  of 0.09 and 0.17, Fig.2 (c). As opposed to top-hat flow above, the flow decays rapidly past this point as it travels further downstream, with the profiles becoming more parabolic, particularly near the jet edge, at  $X/D$  of 0.76. This rapid change in profile is due to the large increase in the boundary layer thickness.

$\delta_{PIV}$  obtained at  $X/D$  of 0.09, is 4.6 mm, which compares well with a theoretical  $\delta$  of 4.9 mm, and is nearly four times larger than the flow where the screens were implemented. Like top hat profile, the fluctuating velocities, Fig.2 (d), show higher values closer to the edge of the jet with a decrease in the centerline. Further downstream, the fluctuating velocity significantly grows, and the difference between the centerline and the edge of the jet decreases.

Table III reports the centerline mean,  $U_c$ , and fluctuating,  $u'_c$ , velocities at similar axial location. These data indicate that the jet with the parabolic initial velocity profile slows down significantly and has higher velocity fluctuations compared to the top hat velocity profile, indicated by the turbulence intensity values. Measurement locations are not exactly the same due to the difference in camera magnification. Diagnostics show that the screens reduce the boundary layer thickness and allows the jet to retain to a top hat velocity profile at the nozzle exit for  $Re = 10,000$ .

**Table III. Jet centerline axial and fluctuating velocities for near-field  $Re = 10,000$  measurements.**

$X/D$	$U_c/U_0$ top hat	$u'_c/U_0$ top hat	$X/D$	$U_c/U_0$ parabolic	$u'_c/U_0$ parabolic
<b>0.09</b>	0.99	0.047	<b>0.09</b>	0.98	0.075
<b>0.20</b>	0.99	0.048	<b>0.17</b>	0.97	0.081
<b>0.53</b>	0.98	0.050	<b>0.54</b>	0.89	0.130
<b>0.75</b>	0.98	0.059	<b>0.76</b>	0.85	0.158

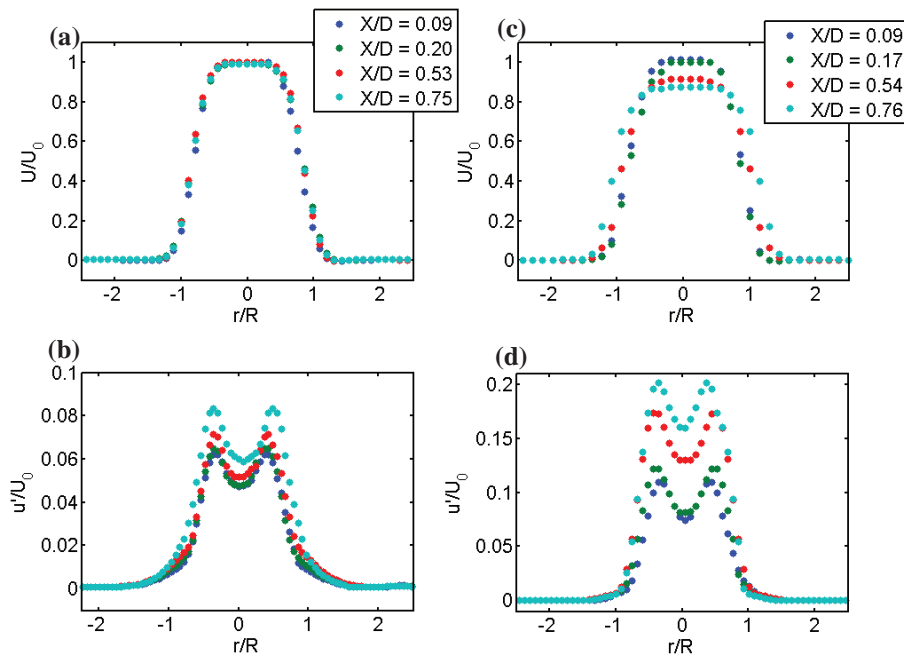


**Figure 2.  $Re = 10,000$  top hat velocity profile (a) axial velocity profile (b) fluctuating velocity profile; and  $Re = 10,000$  parabolic velocity profile (c) axial velocity profile (d) fluctuating velocity profiles**

#### 4. NEAR-FIELD FLOW STRUCTURES

A two dimensional view of a round jet flowing in the axial direction, with a top hat profile at  $Re = 10,000$ , is observed with PLIF. The dye marks the jet issuing from the nozzle (bright region), while the darker stationary fluid surrounds it, Fig.3 (1). Two distinctive vortex rings are initially seen in the flow while a third ring begins to form (a). As these rings travel downstream entraining the surrounding fluid, pairing of the vortex rings initiates (b), and finally merges, while a fourth ring has formed (c). The merged rings travel downstream and the axisymmetric flow breaks down into a three dimensional flow, while the second set of rings begin to pair, along with the formation of another ring (d).

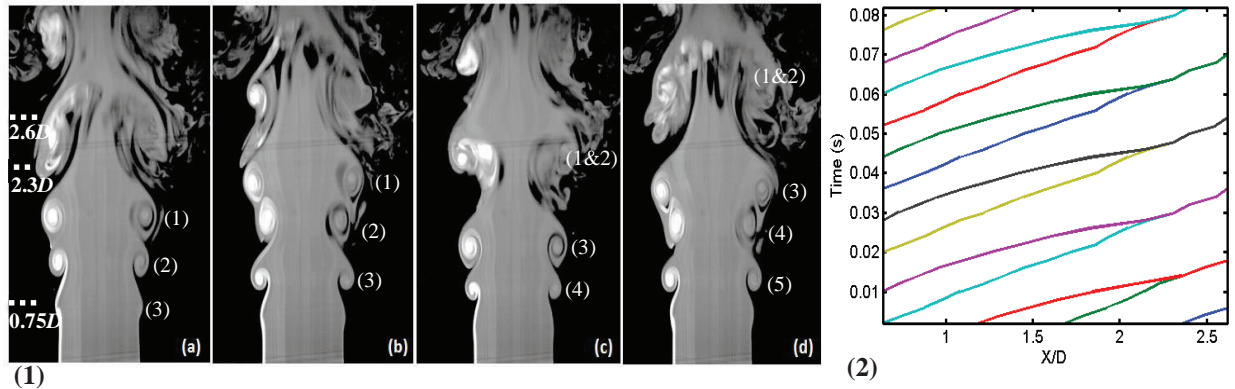


**Figure 3.  $Re = 10,000$  PLIF images with a top hat profile. (1) (a)  $t = 0$  ms, (b)  $t = 6$  ms, (c)  $t = 12$  ms, (d)  $t = 24$  ms. (2) Vortex tracking showing a 125 Hz shedding frequency with a formation at  $0.75D$ , pairing at  $2.3D$  and break down at  $2.6D$**

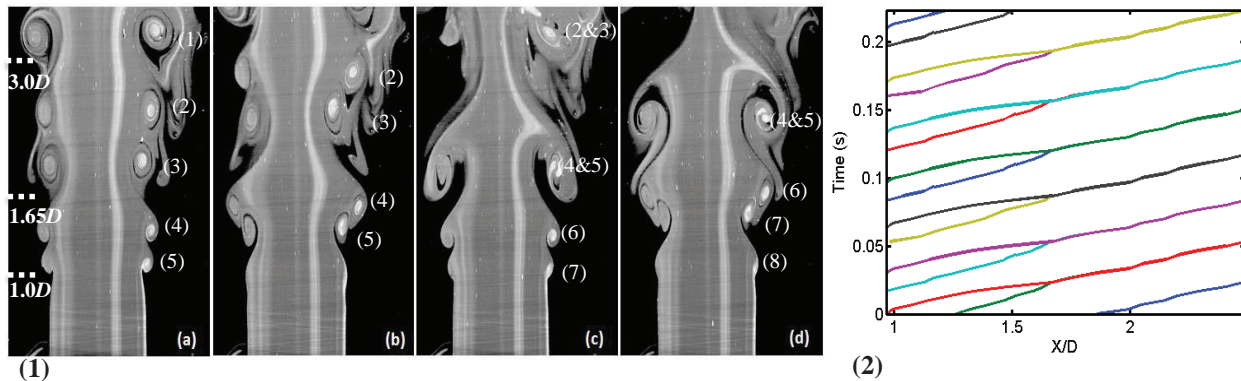


**Figure 4.  $Re = 10,000$  PLIF images with a parabolic profile. (1) (a)  $t = 0$  ms, (b)  $t = 24$  ms, (c)  $t = 42$  ms, (d)  $t = 65$  ms. (2) Vortex tracking showing a shedding frequency at 82 Hz with a formation at  $1.0D$ , pairing at  $1.65D$  and break down at  $3.0D$ .**

With a code developed in Matlab<sup>®</sup>, these rings are monitored over time. The code takes two consequent frames, subtracts the background, and locates the centroid of the vortices from the corrected image. Thus the centroids are "marked" and masks are created to track them, frame by frame, with a cross correlation algorithm that has subpixel accuracy. Fig.3 (2) shows the formation or roll-up of vortex rings, pairing or merging of individual rings, and finally breakdown, where the vortices are no longer coherent structures, as they travel to a position away from the nozzle exit,  $X$ , in relation to  $D$ , where each color represents a single vortex ring. These rings consistently form at a frequency,  $f$ , of 125 Hz at an  $X/D$  of 0.75, and pair or

merge, where two lines intersect, at an  $X/D$  of 2.3, and finally break down at  $X/D$  around 2.6, where 188 vortex pairings over the recording time.

For the same flow rate condition as above PLIF is also acquired for parabolic velocity profile, Fig.4 (1), where the evolution of vortex rings are monitored, Fig. 4 (2). Five distinct vortex rings are visible in a high dye concentration (a). Much like the top hat velocity profile flow structures, the formation of rings,  $f$  of 82 Hz at an  $X/D$  of 1, transpire, where consistent pairing initialize, and the set of vortex rings furthest from the nozzle exit become closer to one another. Merging of rings at the same location,  $X/D$  of 1.65, occurs (c), while the vortex closest to the end of the frame, begins to entrain the ring below it. During the pairing of a second set of rings, the newly combined rings travel downstream as one coherent structure (d). These rings will eventually break down into turbulence at  $X/D$  of 3. For length of data acquired here, this results in 90 vortex ring pairings, which is approximately half of the pairing produced from the top hat velocity profile. The formation of the vortex rings also occurs further from the nozzle exit compared to those issued from a top hat profile, with a much lower shedding frequency. Visually the size of the vortex rings in Fig.4 is larger than those in Fig.3. This qualitatively shows that thin boundary layers increase both the shedding rate and number of vortex pairing occurrences.

A two dimensional cross section of top hat velocity profiled jet initiating in the axial direction for  $Re = 20,000$ , is seen in a high dye concentration, Fig.5 (1). Much like the flow structures for  $Re = 10,000$  top hat profile case, near the nozzle exit two small fully developed vortex rings are visible, which form at evenly spaced time intervals  $f$  of 230 Hz at an  $X/D$  of 0.76 (a). As these rings travel downstream, they entrain the surrounding fluid and begin to merge or combine at  $X/D$  of 1.4(b). The merged vortex rings travel downstream (c) until they break down at  $X/D$  of 1.8 (d), where a second set of rings begin to pair. Approximately 345 vortex ring pairings occur for the 3,000 images acquired.

For the same flow rate with a parabolic velocity profile, the jet flow structures are captured and monitored over time, Fig.6 (1) and (2). The formation of the vortex rings,  $f$  of 120 Hz at an  $X/D$  of 0.9, occurs close to the nozzle exit (a), where these rings initiate pairing (b), and finally merge at an  $X/D$  of 2 (c) and break down into turbulence at an  $X/D$  of 3.1, where approximately 165 vortex pairings occur over the recorded data. Much like the vortex formation for the  $Re = 10,000$  parabolic profile, the rings form and breakdown further downstream compared to the top hat profile at the same  $Re$  case. The shedding frequency is also much slower, which is almost half the shedding frequency of the previous case, and the number of pairings is almost half the number from the top hat profile at the same flow rate, and relatively close in value to the top hat profile at  $Re = 10,000$ . Visually, the vortex rings are larger due to the increase in boundary layer thickness, which is seen in comparing Fig.5 (1) and Fig.6 (1).

PLIF image analysis shows that manipulating the initial velocity profile strongly changes the evolution of the jet flow structures in the near-field. Table III compares the shedding frequency and flow structure characteristics. The shedding frequency significantly decreases with increasing initial boundary layer thickness, and the roll-up of the jets shear layer into vortex rings occurs further from the nozzle exit. The number of vortex pairings for the parabolic velocity profile in the same time cycle decreases to almost half the frequency for the top hat case. The breakdown of rings also occurs further downstream compared to the jet with top hat profile. Visually, the vortex rings are larger in the case where the initial boundary layer thickness is greater from the parabolic profile. Uncertainty analysis based on the measurements taken from the PLIF is calculated using  $\pm 1$  pixels. Assuming a uniformly distributed error contained within the pixel range gives a value of approximately 0.05 mm or  $3 \times 10^{-3}D$  and is considered negligible.

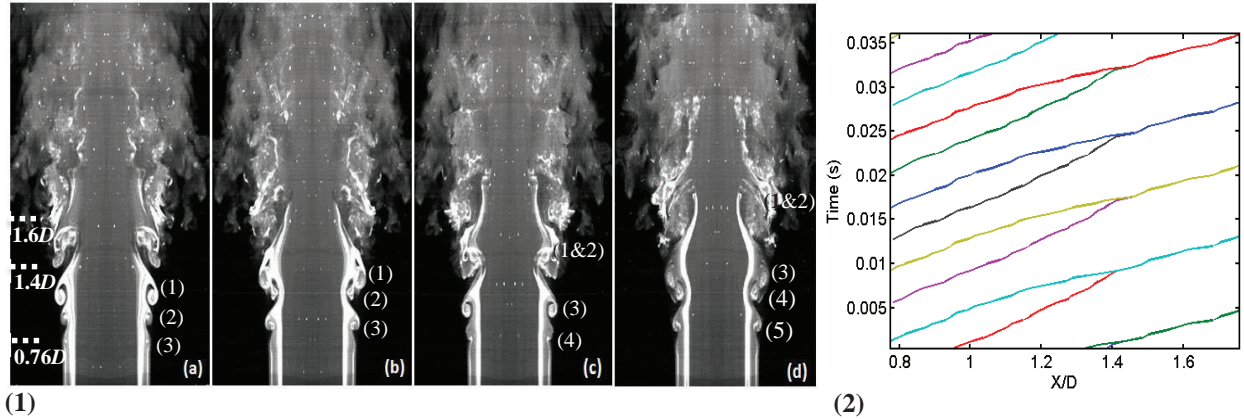


Figure 5.  $Re = 20,000$  PLIF images with a top hat profile. (1) (a)  $t = 0$  ms, (b)  $t = 9$  ms, (c)  $t = 13$  ms, (d)  $t = 22$  ms. (2) Vortex tracking showing a shedding frequency at 230 Hz with a formation at  $0.76D$ , pairing at  $1.4D$  and break down at  $1.8D$ .

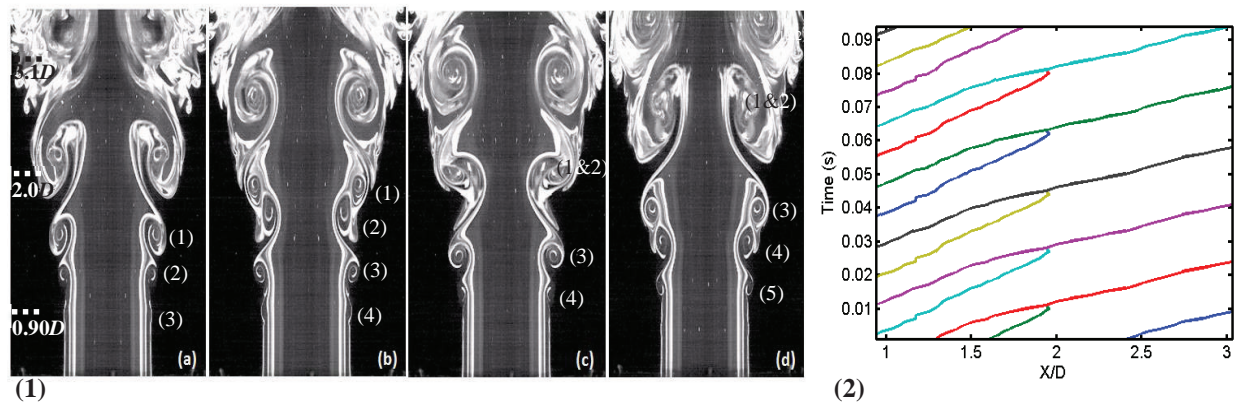


Figure 6.  $Re = 20,000$  PLIF images with a parabolic profile. (1) (a)  $t = 0$  ms, (b)  $t = 6$  ms, (c)  $t = 11$  ms, (d)  $t = 20$  ms. (2) Vortex tracking showing a shedding frequency at 120 Hz with a formation at  $0.90D$ , pairing at  $2.0D$  and break down at  $3.1D$ .

Table IV. Vortex tracking flow evolution for  $Re = 10,000$  and  $20,000$

Re	$f$	Formation	Pairing	Collapse	No. of Pairs
10,000 – top hat	125 Hz	$0.75D$	$2.3D$	$2.6D$	188
10,000 – parabolic	82 Hz	$1.0D$	$1.65D$	$3.0D$	90
20,000 – top hat	230 Hz	$0.76D$	$1.4D$	$1.8D$	345
20,000 – parabolic	120 Hz	$0.90D$	$2.0D$	$3.1D$	165

## 5. SELF-SIMILAR STATISTICS FOR $Re = 20,000$

At  $Re = 20,000$ , two-dimensional velocity fields, measured for both the top hat and parabolic velocity profiles, are characterized in the self-similar region. The centerline velocity,  $U_c$ , is plotted as a function of axial location,  $X$ , where the vertical scale is normalized with respect to  $U_o$ , and the horizontal scale is normalized in relation to  $D$ , Fig.7 (a) The blue points represent the measured velocity values obtained from the first PIV frame, and the black points from the second frame, which are taken at every location along the centerline, approximately  $0.5D$ . The centerline velocity decays inversely proportional to its respective downstream location. This is represented by the solid straight line, and gives a  $B_u$  of 5.7.

Extending this line, in order to intercept the  $x$ -axis, gives the location of the jet virtual origin,  $X_0$ , approximately  $4.1D$ .

The mean axial velocity, normalized by the centerline velocity is graphed against the non-dimensional radial coordinate  $r/(X-X_0)$ , Fig. 7(b). The points represent the measured velocity values obtained from both PIV frames for  $X/D$  from 30 to 50, in steps of 5 nozzle diameters. The mean velocity profile at each location consists of a symmetric Gaussian shape. This confirms that the jet is fully developed or self-similar after  $30D$ .

Reynolds stresses, analyzed at the same measurement locations, are graphed against  $r/(X-X_0)$ , Fig. 7 (c). The symmetric profile of the axial normal stress  $\overline{u^2}$  shows a peak around  $r/(X-X_0)$ , of 0.04 with an rms value of 0.08, and then decreases towards the center of the jet, with an rms value of 0.075. This peak is due to the production of turbulence energy from the Reynolds stress working against the mean shear [15]. The radial profile  $\overline{v^2}$  is symmetrically Gaussian, with a maximum peak in the center of the jet of 0.046. The turbulence shear stress  $\overline{uv}$ , shows a peak,  $r/(X-X_0)$  of 0.04, with an rms value of 0.02, then decreases toward the center of the jet to zero.

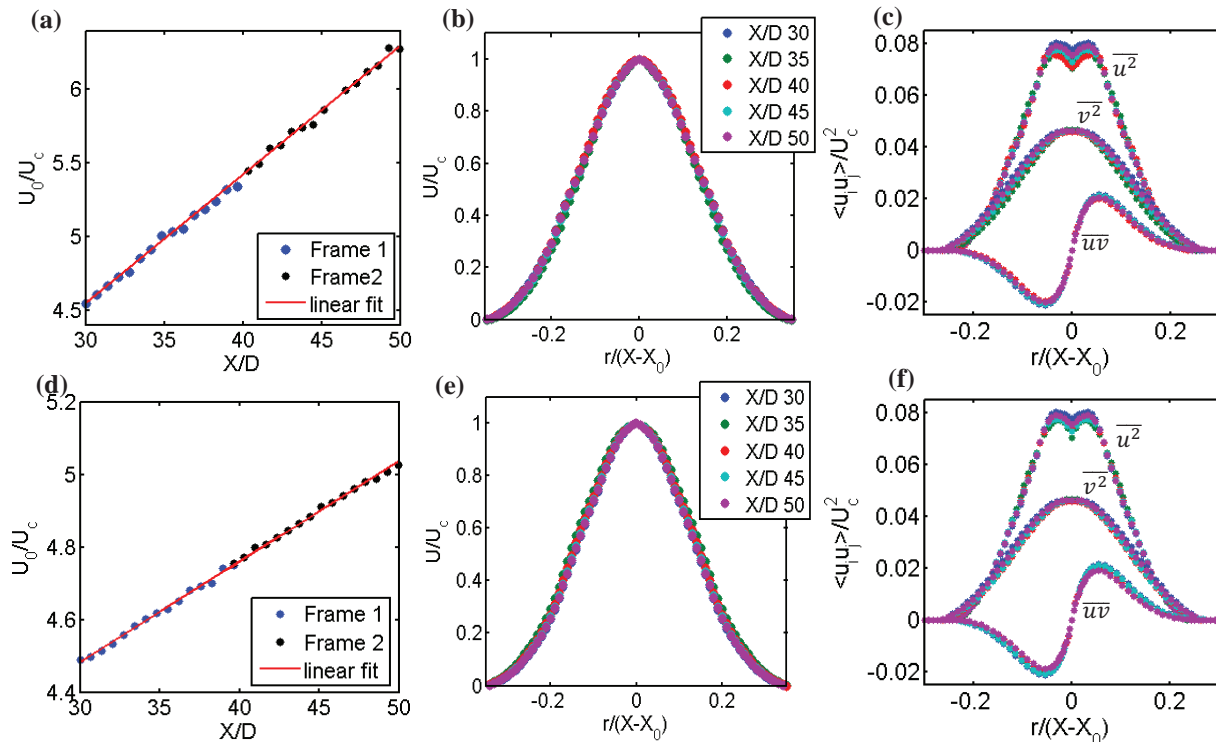


**Figure 7.  $Re = 20,000$  for a top hat profile (a) centerline velocity (b) mean axial velocity profile (c) Reynolds stresses in the self-similar region.  $Re = 20,000$  for a parabolic velocity profile (d) centerline velocity (e) mean axial velocity profile (f) Reynolds stresses in the self-similar region.**

For the jet with a parabolic initial profile, the dimensionless centerline velocity, Fig. 7 (d), also decays proportionally to its location, with  $B_0$  of 6.1 and an  $X_0$  of  $2.2D$ . This indicates that the jet decays faster than the top hat profile, with a 7% slope difference, and a virtual origin much closer to the nozzle exit. Although the jet decays much quicker, the mean axial velocity reaches an identical self-similar state at  $30D$ , Fig. 7 (e), and the Reynolds stresses, at this same measurement locations, show similar profiles at the centerline, Fig. 7 (f), with the dimensionless  $\overline{u^2}$ ,  $\overline{v^2}$ ,  $\overline{uv}$  being 0.076, 0.045, and 0 respectively. Table V shows the comparison for flow characteristics for both the top hat and parabolic profiles.

**Table V. Far-field  $Re = 20,000$  flow characteristics. Average values are reported for  $30D$  to  $50D$  in the jet centerline for Reynolds stresses.**

	Top hat	Parabolic	Hussein et al [15] (Top hat)	Ferdman et al. [11] (Parabolic)
$B_u$	5.7	6.1	5.8	6.4
$X_0$	$4.1D$	$2.2D$	$4.0D$	$2.5D$
$\overline{u^2}/U_c^2$	0.075	0.076	0.076	0.070
$\overline{v^2}/U_c^2$	0.046	0.045	0.047	0.044
$\overline{uv}/U_c^2$	0	0	0	0

The turbulence length scales for the top hat profile,  $\eta$  and  $\lambda$ , in Fig.8 (a) and (b), linearly grows as the flow goes from  $30D$  to  $50D$ . Because the centerline velocity is decaying, the length scales tend to grow as the flow dissipates.  $Re_\lambda$ , Fig.8 (c), decreases in relation to its downstream position. This is due to both the decaying velocity fluctuation and increase in size of  $\lambda$ .

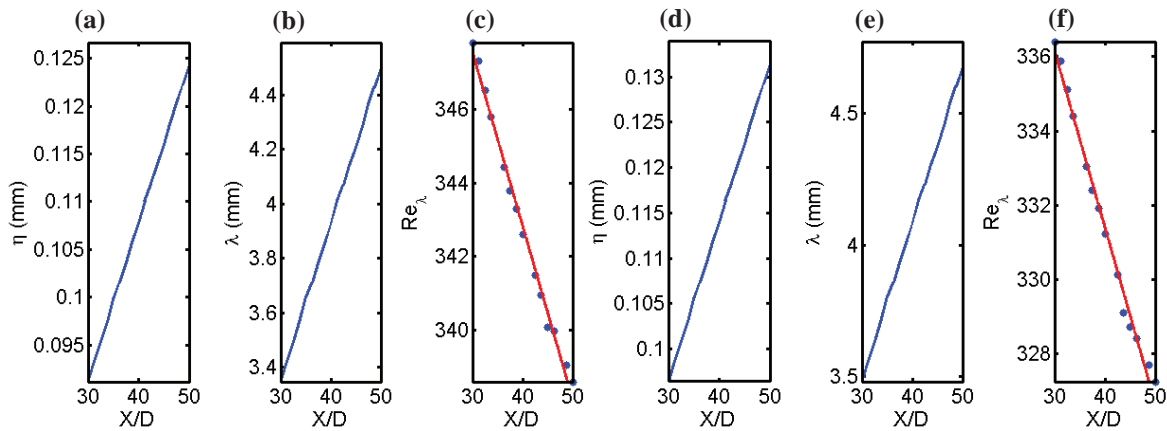


**Figure 8. Turbulence length scale estimation for  $Re = 20,000$  with a top hat velocity profile (a) Kolmogorov length scale (b) Taylor microscale (c) Taylor-scale Reynolds number, and with a parabolic velocity profile (d) Kolmogorov length scale (e) Taylor microscale (f) Taylor-scale Reynolds number**

The turbulence length scales for the parabolic profile also behave in a similar manner, with increasing  $\eta$  and  $\lambda$ , Fig.8 (d) and (e). Although the behavior is similar to the top hat profile, the size of each scale is slightly larger. This is due to the higher centerline velocity decay rate.  $Re_\lambda$ , Fig.8 (f), also decreases in relation to its downstream position, but is slightly smaller in value due to the higher decaying velocity fluctuation. Table VI compares the length scale sizes for both profiles at  $30D$ ,  $40D$ , and  $50D$ .

Analysis indicates that the parabolic velocity profile has a centerline velocity which decays quicker than the top hat profile due to the increase in boundary layer initiated from the nozzle exit. Although the slope of centerline velocity and the virtual origin are comparatively different, the flow still reaches the same self-similar state 30 nozzle diameters downstream of jet initiation, and has similar velocity fluctuations at the same measurement locations for both initial velocity distributions. Slight differentiation in length scales between profiles exists due to the increase in the velocity decay slope, which causes both the Kolmogorov and the Taylor scales to be slightly larger.

**Table VI. Far-field  $Re = 20,000$  length scale comparison for both initial velocity top hat and parabolic profiles**

$X/D$	$\eta$ Top hat	$\eta$ Parabolic	$\lambda$ Top hat	$\lambda$ Parabolic	$Re_\lambda$ Top hat	$Re_\lambda$ Parabolic
30	0.09 mm	0.10 mm	3.34 mm	3.47 mm	348	337
40	0.11 mm	0.12 mm	3.92 mm	4.08 mm	343	332
50	0.13 mm	0.13 mm	4.59 mm	4.77 mm	339	327

## 6. INDEX MATCHED FLOW FACILITY CHARACTERIZATION

While numerous studies have been conducted on round jets injected into a homogeneous quiescent fluid, few studies focus on jets discharging in stratified environments. This absence of data is due to the difficulty in resolving velocity fields in variable density environments [19]. In fluids, the index of refraction changes with density. While conducting non-intrusive imaging diagnostics as with PLIF or PIV, the laser sheet, used to illuminate the flow bends as it passes through a medium of varying refractive index. Light scattered from the seeding particles or florescent dye through a non-uniform refractive index will result in blurred or distorted images. Experimental research has shown that an index difference as small as 0.0002 is significant enough to alter data [20].

To overcome this imaging difficulty, the experimental facility will be modified to produce a buoyant jet injected into a stratified environment using index matched fluids, at  $Re = 20,000$ . This allows for the development of non-intrusive diagnostics without optical aberrations.

## 7. CONCLUSIONS

Controlling the initial conditions of a round, axisymmetric, and incompressible jet at  $Re = 10,000$  and  $20,000$ , shows that flow formation and evolution are extremely sensitive to these conditions. Near-field PLIF evaluation of the vortex rings shed from the jet shear layer shows that the parabolic velocity profiles has a vortex shedding frequency decrease, which is approximately half of those initiated with a top hat profile for the same flow rate. An increase in location of vortex ring formation and breakdown with the parabolic profile is observed, as well as increase in vortex ring size. This increase is a result of boundary layer growth at the nozzle exit, shown in the mean axial velocity profiles in the near-field analysis.  $Re = 10,000$  axial velocity profiles show a jet that initially retains a top-hat profile, then dramatically alters and becomes parabolic less than  $1D$  downstream for the parabolic case. Far-field analysis for  $Re = 20,000$  indicates velocity decays for the parabolic profile at a faster rate and has a virtual origin closer to the nozzle exit, but still reaches self-similarity  $30D$  downstream. Length scale investigation shows slightly larger Kolmogorov scale and Taylor microscale due to the increase in slope of the centerline velocity decay. These data will provide baseline to study a buoyant jet injected into a stratified environment with non-intrusive optical diagnostics in an index matched environment to minimize optical aberrations.

## ACKNOWLEDGMENTS

This project was partially supported with a DOE NEUP grant.

## REFERENCES

1. G. Bruneaux, "A study of mixture formation in direct injection diesel like conditions using quantitative fuel concentration visualizations in a gaseous fuel jet," SAE International (2002).

2. B. J. Balakumar and R. J. Adrian, "Particle-image velocimetry measurements in the exhaust of a solid rocket motor," *Experiments in Fluids*, 36, 166-175 (2004).
3. D. J. Zboray, "Toward CFD-grade database addressing LWR containment phenomena," *Nuclear Engineering Design*, 253, 331-342 (2012).
4. D. Liepmann and M. Gharib, "The role of streamwise vorticity in the near-field entrainment of round jets," *Journal of Fluid Mechanics*, 245 (1992).
5. B.J. Bayly, S.A. Orszag, T. Herbert "Instability mechanisms in shear flow transition," *Annual Review of Fluid Mechanics*, 20, 359-391 (1988).
6. M. Ho and L. S. Huang, "Subharmonics and vortex merging in mixing layers," *Annual Review of Fluid Mechanics*, 119 (1982).
7. D. Lannes, "A stability criterion for two-fluid interfaces and applications," *Archive for Rational Mechanics and Analysis*, 208, pp. 481-567 (2013).
8. R. Fox, P. Pritchard, A. McDonald, "Introduction to fluid mechanics," 7<sup>th</sup> edition, John Wiley & Sons, Inc., Hoboken, NJ (2009)
9. W. George, "The self-preservation of turbulent flows and its relation to initial conditions and coherent structures," *Advances in Turbulence*, pp. 39-73 (1989).
10. W. Quinn, "Experimental study of the near field and transition region of a free jet issuing from a sharp-edged elliptic orifice plate," *European Journal of Mechanics B. Fluids*, 26, 583-614 (2007).
11. E. Ferdman, M.V. Otugen, S. Kim, "Effect of initial velocity profile on the development of round jets," *Journal of Propulsion and Power*, 16, pp. 676-686 (2000)
12. J. Mi, P. Kalt, G.J. Nathan, C.Y. Wong, "PIV measurements of a turbulent jet issuing from round sharp-edged plate," *Experiments in Fluids*, 42, pp. 625-637 (2007).
13. G. Xu and R. Antonia, "Effect of different initial conditions on a turbulent round free jet," *Experiments in Fluids*, 33, 677-683 (2002).
14. A.B. McCleney, "Experimental Study of Axial Forcing on a Jet," M.S. Thesis. Department of Mechanical and Aerospace Engineering, The George Washington University (2012).
15. H.J., Hussein, S.P., Capp, W.K., George, "Velocity measurements in a high-Reynolds-number, momentum-conserving, axisymmetric, turbulent jet," *Journal of Fluid Mechanics*, 258, pp. 31-75 (1994).
16. J. H. Bell and R. D. Mehta, "Boundary-layer predictions for small low-speed contractions," *AIAA Journal*, 27, 372-374 (1989).
17. G.K. Batchelor, "On the concept and properties of the idealized hydrodynamic resistance." ACA Report 13, 1-15 (1945).
18. S. Pope, "Turbulent Flows," Cambridge University Press." First edition. (2000).
19. M. K. Roberts, K. Maile, G. Daviero, "Mixing of jets in stratified fluids," *Journal of Hydraulics Engineering*, 127, 1-7 (2001).
20. A. Alahyari and E. Longmire, "Particle image velocimetry in a variable density flow: application to a dynamically evolving microburst," *Experiments in Fluids*, 17, 434-440 (1994).